SIAM J. Appl. Math.
Vol. 72, No. 4, pp. 1192–1212

MULTIPLE SHEAR-BANDING TRANSITIONS FOR A MODEL OF WORMLIKE MICELLAR SOLUTIONS*

LIN ZHOU†, L. PAMELA COOK‡, AND GARETH H. MCKINLEY§

Abstract. Wormlike micelles are long wormy cylindrical aggregates of surfactants, self-assembled within a solvent, which entangle and continuously break and reform at thermal equilibrium. Rheological characterization and flow visualization experiments with micellar solutions show that under steady state shearing flow the deformation field may not remain homogeneous but instead spatially localize, resulting in the formation of pronounced shear bands. Models which capture this banding behavior generally display a nonmonotonic constitutive response or "flow curve" (of the shear stress resulting from the imposed shear rate). Homogeneous steady state solutions along the decreasing portion of this constitutive curve are unstable and, under shear rate control, the solution in this regime bifurcates to a spatially inhomogeneous flow with two shear rates selected from the positive slope portions of the curve that coexist at identical values of the stress. Tracking of the spatio-temporal development of the banded solution structure shows a strong elastic recoil in the local fluid velocity profile at short times (earlier than the effective relaxation time of the entangled chains). At longer times the velocity profile approaches its steady banded state. These predictions agree with experimental observations by Miller and Rothstein [*J. Non-Newtonian Fluid Mech.*, 143 (2007), pp. 22–37]. In this paper the interplay of the competing roles of inertia, the imposed shear rate, and the transient dynamics of the start up in the flow are examined using the VCM (Vasquez–Cook–McKinley) model. This constitutive model is a scission/reforming network model developed to capture the essential physics of the deformable micellar microstructure and its coupling to the macroscopic flow field. The addition of inertia into the coupled set of nonlinear partial differential equations describing the material response changes the type of the equation set, introducing a transient damped (diffusive and dispersive) inertio-elastic shear wave following the imposition of flow. Depending on the relative time scales associated with the damping, the shear wave speed, the start-up ramp speed, and the imposed shear rate, the reflections of the damped transient wave from the boundaries can interfere with the microscopic mechanisms leading to elastic recoil and the localization of the shear that leads to formation of a shear band. The result of this interference is the establishment of a transient velocity profile with a varying number of (two, three, or four) shear bands. When there is no stress diffusion in the model the multiple-banded profile exists to steady state, and the resulting macroscopic flow is thus not uniquely specified by the imposed shear rate alone.

Key words. complex fluids, inertial effects, multiple shear bands

AMS subject classifications. 76A05, 76A10, 35Q35

DOI. 10.1137/120863113

1. Introduction.

Wormlike micelles are long wormy cylindrical aggregations of micelles formed under appropriate concentration, salinity, and temperature conditions as amphiphilic surfactant molecules "hide" their hydrophobic tails from the aqueous solvent phase. This specific class of complex fluid is used widely in shampoos and other personal care products as well as in enhanced oil recovery operations due to the combination of desired rheological properties such as high viscosity at low shear rates, strong shear thinning as the shear rate increases, and pronounced change in properties as the conditions (e.g., concentration, salinity, temperature) change. By

*Received by the editors January 3, 2012; accepted for publication (in revised form) May 30, 2012; published electronically August 21, 2012.
http://www.siam.org/journals/siap/72-4/86311.html
†Department of Mathematics, New York City College of Technology, CUNY, Brooklyn, NY 11201 (lzhou@citytech.cuny.edu).
‡Department of Mathematical Sciences, University of Delaware, Newark, DE 19716 (cook@math.udel.edu).
§Department of Mechanical Engineering, MIT, Cambridge, MA 02139 (gareth@mit.edu).

careful control of salinity, the worms can become long enough to entangle and thus impart significant elastic properties to the fluid, but they also continuously break and reform due to thermal fluctuations leading to viscoelastic stress relaxation [33]. This scission/reforming process adds an extra time scale to the flow in addition to Rousian and reptative (i.e., "snake-like" curvilinear diffusive motions along the worm backbone) relaxation mechanisms. The microstructure of the fluid consists of an entangled network of these wormlike structures which are long enough and sufficiently long-lived that their microstructural characteristics (alignment and stretching) can affect the macroscopic flow and vice versa. In experimental observations of shearing flows, wormlike micellar solutions show spatially inhomogeneous flow (shear banding) at high shear rates even in steady simple shearing situations. For example, in a cylindrical Couette flow beyond a critical shear rate, a high shear rate band develops near the inner rotating cylinder and a low shear rate band forms towards the outer, stationary cylinder [35]. Correspondingly, the "flow curve," that is, the shear stress measured at the inner cylinder as a function of the applied shear rate, shows a plateau for the range of shear rates over which banding is observed. Reviews on experimental results and modeling of wormlike micellar solutions can be found in Cates and Fielding [9], Rehage and Hoffman [33], Lerouge and Berret [22], and Fardin et al. [18] among others.

A number of different viscoelastic constitutive equations have been proposed for describing the shear banding properties of wormlike micellar solutions under different imposed flow conditions. A single species phenomenological model, the Johnson–Segalman model, has been investigated extensively for modeling the banding observed in shearing deformations [23, 28, 31], but this model suffers from the following: (1) having to use an unphysically large solvent viscosity to quantitatively fit data and (2) failing to adequately describe flows of micelles in other flow situations such as step strain or extension. Other single species models that have been investigated include the PEC model [41] and the Rolie–Poly model [2]. These models also suffer from various technical drawbacks (see [11, 40] for related discussion). Recently, a more complex two-species model (the Vasquez–Cook–McKinley (VCM) model) has been proposed which incorporates the scission and reforming of the micellar chains as well as the coupling between the local stress and number density of each species. Several analytically simpler limiting variants of this model, the PEC and PEC+M models, have been explored in time-dependent inhomogeneous cylindrical Couette flow [41]. Spatially inhomogeneous and transient responses of the VCM model have been studied in Large Amplitude Oscillatory Shear (LAOS) flow in a cylindrical Couette device [40], in a one-dimensional extensional flow [11], and in pressure-driven channel flow [12, 13].

The VCM [38] model is a constitutive model or *rheological equation of state* that has been formulated to describe the flow behavior of wormlike micellar solutions under a broad range of imposed deformation histories. It was derived self-consistently from the dynamical equations governing the evolution of species distributions in configuration space involving, for simplicity, only two species; species A, of length L, which can break at its midpoint to form two shorter worms (species B), each of length L/2. In configuration space, the number density distributions of each species Ψ_A, Ψ_B, respectively, are functions of the physical location of the center of mass $\mathbf{r}$, the end-to-end vector of the worm $\mathbf{Q}$, and time t.

Solutions to the one-dimensional inertialess Johnson–Segalman, PEC, PEC+M, and VCM models in steady shear flow within a cylindrical Couette geometry show

that at low imposed shear rates the kinematics are homogeneous and there is no shear banding. Beyond a (model-dependent) critical shear rate the flow bifurcates so that there are typically two shear bands with different characteristic shear rates (although for very small curvatures [28] has reported existence of a three-banded inertialess solution). The banding behavior occurs because the constitutive equations predict a nonmonotone flow curve (of stress versus shear rate) under the assumption of homogeneous unidirectional flow. The constitutive curve is monotone increasing for small and large shear rates, but is locally decreasing for a range of shear rates, $\dot{\gamma}_1 < \dot{\gamma} < \dot{\gamma}_2$. Homogeneous flows in the decreasing portion of the constitutive curve are unstable. When the shear rate is allowed to vary spatially, the flow transitions to a shear banded state with the two selected shear rates, both being on stable portions of the flow curve [18, 40]. The linear stability of the banded flow has been examined for several constitutive models including the VCM model [12, 39]. It has been shown that the models have an unstable domain for sufficiently small values of the (suitably nondimensionalized) stress-induced diffusion parameter. As this parameter increases in relative magnitude (for example, through a decrease in the characteristic geometric dimensional scale), the flow stabilizes.

Although the VCM model results compare well with experiment in a qualitative sense, and offer the advantage over single species models in that they account for the spatio-temporal change of the number density (of each species), quantitative agreement has room for improvement [30]. Wormlike micelles can break at any point along their length, and thus a model that incorporates continuous breakage rates (along the length of the wormlike micelle) would be an improvement over the VCM model which only enables the micelle to break and reform at its midpoint. This would substantially increase the computation complexity.

Most investigations into shear banding up to now have examined steady state solutions which show a single kink, that is, a "two-banded" structure. Studying the initial transient flow, onset of shear localization and approach to the steady state flow profile provides more insight into the evolution of flow structure. Several authors have carried out flow visualization experiments on the transient response of wormlike micellar fluids following start up of shear flow in a cylindrical Couette cell [4, 7, 14, 25, 27] and a number of reviews have also been compiled [8, 22, 29]. In at least two of these experiments [14, 27] transient damped inertio-elastic shear waves were observed propagating across the Couette cell and in at least one of these studies, multiple shear banded states (i.e., more than one kink in the velocity across the gap) were observed in the final steady state flow profile. A three-banded structure was also observed for triblock copolymer micellar mixtures in [24]. While other experimenters have not reported multiple-banded states, we show in our analysis that their existence depends critically on the magnitude of several parameters which characterize the precise form of the rheological response in the system. As we show below using numerical calculations, experiments with the same fluid, but in a different experimental apparatus (for example a narrower rheometer gap or a slower initial ramp up) may not lead to the multiple-banded states. Both the experiments showing the inertio-elastic shear waves and recent computer simulation of the VCM model in LAOS (another rapid time-varying flow) show interesting spatio-temporal dynamics [40]. These reports indicate that inertial effects at short times may well play a role in the formation of the shear bands. In order to further investigate this hypothesis, in this paper we include inertia in the VCM equation set and investigate the resulting evolution of multiple-banded configurations towards steady state.

Denn and Porteous [15] examined the effect of inertia on transient flow predictions for start-up of steady shear flow of the upper convected Maxwell model (UCM model) in a bounded domain. The UCM model exhibits a monotone stress/shear-rate constitutive curve and hence does not describe shear banding. They determined that the spatio-temporal evolution of the velocity is governed by a damped wave equation representing the propagation and damping of an inertio-elastic shear wave. In start up of shear flow, the coupling of fluid inertia and viscoelastic stress growth results in a propagating wave front with a nominal wave speed given by $c' = \sqrt{G/\rho}$, where G is the shear modulus and ρ is the fluid density. Tanner [36] considered the analogous problem in a semi-infinite domain (the Rayleigh problem) and also explored the additional diffusive effects of a viscous solvent (i.e., the Oldroyd-B model) on the sharpness of the propagating shear wave.

As we show below for the VCM constitutive model, the transient inertio-elastic shear wave resulting from coupling of elastic stresses and fluid inertia can cause changes to the shear-localization processes that lead to the ultimate "banded" velocity profile. In the limiting case of negligible stress diffusion these changes persist to the final steady state, and the flow profile is thus no longer uniquely determined by the imposed wall shear rate. The evolution in the banding behavior, and the corresponding plateau in the flow curve, depend on the history of the flow, in particular how the shear flow was initiated (a fast or slow ramp up to the final wall velocity). This memory effect has also been reported in the shear flow predictions of the PEC and Johnson–Segalman models [1, 41], but is more pronounced in the VCM model. We show below that because of this dependence on the deformation history, the interaction between the shear wave (and its subsequent reflections from the walls of the device) with the spatially developing flow profile can generate multiply-banded solutions in transient and even steady state shear flows. This is of particular interest because, as reported above, several experiments [14, 24, 27] have shown multiple-banded solutions in Taylor–Couette flow. Also, in weakly nonviscometric geometries (for example, a cone plate geometry), shear flows of wormlike micellar fluids can display a three-banded profile [8, 16].

The present paper is a computational study of the nonlinear coupled partial differential equation system (the VCM model together with conservation of mass and momentum) describing flows of wormlike micellar mixtures. Along with this we provide a descriptive analysis of a simpler (quasi-linear) model (the Oldroyd-B model) to help explain and motivate the results for the nonlinear model. We first review the initial-boundary value problem for the VCM model. This is followed by a description of the influence of inertia on the solutions of the simpler, quasi-linear, Oldroyd-B (O-B) model; then we give an analysis of the inertial effects on the full nonlinear VCM model in shear. The particular prediction of interest is that multiple banding regimes (comprising three or four shear bands) occur in certain regions of parameter space. We explore the role of fluid inertia and ramp time on determining the boundaries of the regimes describing these multiple-banded states.

2. Governing equations. The VCM model equations begin in configuration space where the number density distribution functions for each of the two species A, B are $\psi_A(\mathbf{r}, \mathbf{Q}, t), \psi_B(\mathbf{r}, \mathbf{Q}, t)$, respectively. The governing equations for the number density distribution functions are formulated as evolution equations incorporating a Hookean connector spring force, Brownian motion, and convection. Here $\mathbf{r}, \mathbf{Q}, t$ are, respectively, the physical space coordinate, the end-to-end vector of the wormlike micelle, and time. Integration of the number density distribution functions

over configuration space yields the number density of each species in physical space $n_A(\mathbf{r},t), n_B(\mathbf{r},t)$. The second moment of each distribution function is proportional to the stress [6]. After nondimensionalization [38], the resulting equations for these variables are

$$\mu\frac{Dn_A}{Dt} = 2\delta_A\nabla^2 n_A - \delta_A\nabla\nabla : \mathbf{A} + \frac{1}{2}c_2 n_B^2 - c_1 n_A, \tag{1}$$

$$\mu\frac{Dn_B}{Dt} = 2\delta_B\nabla^2 n_B - 2\delta_B\,\nabla\nabla : \mathbf{B} - c_2 n_B^2 + 2c_1 n_A, \tag{2}$$

$$\mu\mathbf{A}_{(1)} + \mathbf{A} - n_A\,\mathbf{I} - \delta_A\nabla^2\mathbf{A} = c_2\,n_B\,\mathbf{B} - c_1\mathbf{A}, \tag{3a}$$

$$\epsilon\mu\mathbf{B}_{(1)} + \mathbf{B} - \frac{n_B}{2}\,\mathbf{I} - \epsilon\delta_B\nabla^2\mathbf{B} = -2\epsilon\,c_2\,n_B\,\mathbf{B} + 2\epsilon\,c_1\mathbf{A}, \tag{3b}$$

where the subscript (1) denotes the upper convected derivative [41]. Here $\mathbf{A}$ and $\mathbf{B}$ are the nondimensional stress associated with each species and c_1, c_2 are the breakage rate of the long worms and the reforming rate of the short worms, respectively. These rate constants describe the nonlinear evolution of the viscoelastic stress in the entangled network and can be chosen based on the microstructural physics of the material under study. In the VCM model for entangled network of wormlike micelles we chose $c_1 = c_{1eq} + \frac{\mu\xi}{3}\dot{\boldsymbol{\gamma}} : \mathbf{A}$ and $c_2 = c_{2eq}$, where c_{1eq}, c_{2eq} are the constant equilibrium values [38].

These constitutive equations are coupled to the equations of conservation of mass,

$$\nabla\cdot\mathbf{v} = 0, \tag{4}$$

and conservation of linear momentum,

$$E^{-1}\frac{\partial\mathbf{v}}{\partial t} = -\nabla\cdot(P\mathbf{I} - \beta\dot{\boldsymbol{\gamma}} + \boldsymbol{\tau_p}). \tag{5}$$

Here $\boldsymbol{\tau_p} = (n_A + n_B)\mathbf{I} - \mathbf{A} - 2\mathbf{B}$, and $\dot{\boldsymbol{\gamma}} = \nabla\mathbf{v} + (\nabla\mathbf{v})^T$ is the strain rate tensor. The dimensionless parameter $E = \lambda_{eff}\eta_p/\rho H^2 = G_0\lambda_{eff}^2/\rho H^2$ is an elasticity number that compares the effective relaxation time of the fluid λ_{eff} with the inertial diffusion time $t'_{idiff} \sim \rho H^2/\eta_p$, which is nonzero due to the presence of inertia. For typical "wide" gaps in a macroscopic rheometer (e.g., a 3mm gap) and a representative micellar fluid, for example, $\rho \sim 1045kg/m^3$, $G_0 = 22.4Pa$, $\lambda = 0.35s$, evaluation of the elasticity number gives $E \sim O(10^2 - 10^3)$ [14]. The ratio $\beta = \eta_s/\eta_p$ is the ratio of solvent viscosity (typically water) to the zero shear rate viscosity of the micellar solution and is typically very small (e.g., for a common micellar fluid, we fit a value $\beta = 7\times10^{-5}$ [41]). The nondimensional diffusion constant δ_α is defined as $\delta_\alpha = \lambda_A D_\alpha/H^2$ for species $\alpha = A, B$, where λ_A is the reptation time of species A, D_α is the self diffusion time of species α, and H is the characteristic geometric length scale of the flow. We take $\delta_A = \delta_B = \delta$ for simplicity. Typical values of δ are $O(10^{-3})$ or smaller, but we note that the magnitude of δ is dependent on the scale of the geometry so that in a microchannel in which $H = 10^{-4}$ m, δ is much larger, $O(10^{-1})$ [13]. Note that for typical micellar fluids we expect $\delta \ll E\beta$.

In this paper we consider the canonical rheological experiment of the start up of steady shear flow. The flow starts from a well-defined rest condition so that at

$t = 0$, $\boldsymbol{\tau_p} = 0$ and $\mathbf{v} = 0$. Because in a real device, the moving wall (e.g., the inner wall in a Taylor–Couette device) cannot jump instantaneously to its final velocity; for simplicity the functional form $v_i = De\tanh(at)$ is used as the velocity boundary condition at the inner wall, while the outer wall is held fixed, $v = 0$. The parameter a controls how rapidly the wall velocity approaches steady state [41]. Here $De = \lambda_{eff}U/H$, where U is the dimensional imposed wall velocity. The corresponding boundary conditions on the number density and stress equations are no flux through the solid walls [5, 10, 17, 28].

Before considering the time-dependent solutions of the VCM model, we show the inertialess steady state flow curve (Figure 1) evaluated under shear-rate-controlled conditions in a circular Couette rheometer. The shear stress is computed at the inner cylinder, and the shear rate is the apparent shear rate across the gap (the velocity of the inner cylinder divided by the gap width since the outer cylinder is held fixed). For shear rates corresponding to the increasing portions of the flow curve, the velocity profile is almost linear, while along the plateau in the flow curve the velocity profile shows a two-banded solution with a high shear rate region ($\dot{\gamma}_1$) near the inner moving wall and a low shear rate region ($\dot{\gamma}_2$) near the outer stationary wall. Unlike other single species models, the high shear rate portion of the two species VCM model flow curve is dominated by the short viscoelastic species, B (all the long worms of species A having broken), as opposed to arising only from an underlying purely viscous solvent.

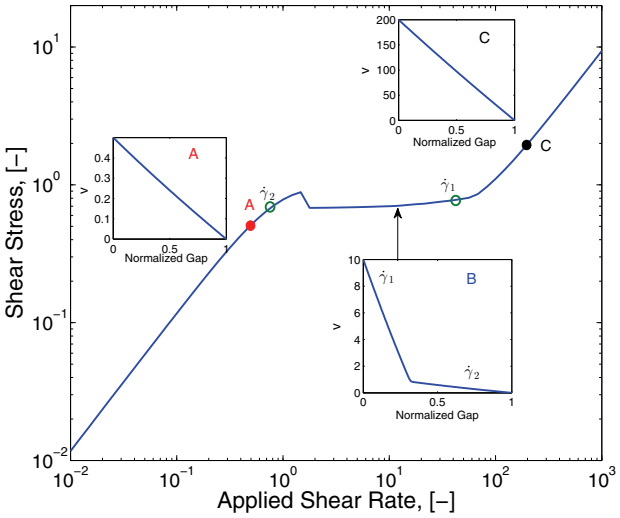

FIG. 1. *Steady state flow curve of the inertialess VCM model with diffusion ($\delta = 0.001$). The simulation is in circular Couette flow with inner radius $r_i = 10$, outer radius $r_o = 11$, so the curvature $p = (r_o - r_i)/r_i = 0.1$. The model parameters are $\xi = 0.7$, $\mu = 5.7$, $\epsilon = 4.5 \times 10^{-4}$, $n_B^0 = 1.3$, and $\beta = 6.8 \times 10^{-5}$. The insets are typical velocity profiles along the two increasing parts of the curve and in the plateau region, respectively.*

There are five distinct dimensional time scales in the transient evolution equations, namely λ_{eff}, the effective relaxation time; $t'_{flow} = 1/\dot{\gamma} = H/U$, the convective flow time scale; $t'_{idiff} = \rho H^2/\eta_p$, the inertial time scale; $t'_{\delta} = H^2/D_A$, the diffusive time scale for number density and stress; and $t'_{ramp} = \lambda_{eff}/a = 1/a'$, the time scale for the imposed boundary condition. From these five time scales we can define four

corresponding dimensionless groups: $De = \lambda_{eff}/t'_{flow} = \lambda_{eff}\dot{\gamma}$, $E = \lambda_{eff}/t'_{idiff} = \lambda_{eff}\eta_p/\rho H^2$, $\delta = \lambda_{eff}/t'_{\delta} = \lambda_{eff}D_A/H^2$, and $a = \lambda_{eff}/t'_{ramp}$. In experiments, the machine ramp time and the precise functional form of the start-up transient will vary with the rheometer design. One simulation of the motor response [30] suggests that a reasonable dimensional ramp rate of $a' \approx 25s^{-1}$. For an effective relaxation time $\lambda_{eff} \sim O(1s)$ as in [27], we thus consider in our computations appropriate values of the dimensionless ramp time scale to be $a \sim 10 - 100$.

The nonlinear equations (1)–(3) and (5) together with the initial and boundary conditions indicated above are solved using the method of lines (MOL) with the spatial variable discretized by the Chebyshev spectral method. The resulting system of differential-algebraic equations is solved in time using the $Ode15s$ Solver in MATLAB.

3. Oldroyd-B model with fluid inertia. Before we study the interaction of the inertio-elastic wave with the formation of the shear bands in the (nonlinear) VCM model, we first discuss and review the simpler, upper convected Maxwell model with the addition of a viscous solvent (i.e., the Oldroyd-B model (O-B)), with inclusion of fluid inertia and viscoelastic stress diffusion [3, 17, 20, 32]. For this single species model, the number density is a constant and the extra stress is given (in dimensionless form) by $\boldsymbol{\tau} = -(\mathbf{A} - \mathbf{I}) - \beta\dot{\boldsymbol{\gamma}}$. The constitutive equation for the second rank configuration tensor $\mathbf{A}$ incorporating stress diffusion is then

$$\mathbf{A}_{(1)} + \mathbf{A} - \mathbf{I} - \delta\nabla^2\mathbf{A} = \mathbf{0}. \tag{6}$$

In a simple rectilinear shearing flow the flow is in the x direction and the velocity depends only on the y direction, i.e., $\mathbf{v}(x, y, t) = (v(y, t), 0, 0)^T$. This flow automatically conserves mass and the evolution equations for the nonzero components of the stress field and velocity are given by

$$\frac{\partial A_{xy}}{\partial t} = \delta\frac{\partial^2 A_{xy}}{\partial y^2} - A_{xy} + \frac{\partial v}{\partial y}A_{yy}, \tag{7a}$$

$$\frac{\partial A_{xx}}{\partial t} = \delta\frac{\partial^2 A_{xx}}{\partial y^2} - A_{xx} + 1 + 2\frac{\partial v}{\partial y}A_{xy}, \tag{7b}$$

$$\frac{\partial A_{yy}}{\partial t} = \delta\frac{\partial^2 A_{yy}}{\partial y^2} - A_{yy} + 1, \tag{7c}$$

$$E^{-1}\frac{\partial v}{\partial t} = \frac{\partial A_{xy}}{\partial y} + \beta\frac{\partial^2 v}{\partial y^2}. \tag{7d}$$

The equilibrium initial conditions and the evolution equation (7c) assure that $A_{yy} \equiv 1$ for all times. Substitution of this value into (7a) yields two coupled equations (7a) and (7d) for the unknowns A_{xy} and v. The streamwise normal stress A_{xx} can then be solved for subsequently. Differentiation of (7d) with respect to t and of (7a) with respect to y to eliminate A_{xy} from the equations yields the following governing equation for the velocity:

$$\frac{\partial^2 v}{\partial t^2} + \frac{\partial v}{\partial t} = -E\delta\beta\frac{\partial^4 v}{\partial y^4} + (\delta + E\beta)\frac{\partial^3 v}{\partial y^2\partial t} + E(\beta + 1)\frac{\partial^2 v}{\partial y^2}. \tag{8}$$

When there is no diffusion and no solvent, $\delta = \beta = 0$, the constitutive equation reduces to that of the Maxwell model (UCM) and the evolution equation simplifies to

$$\frac{\partial^2 v}{\partial t^2} + \frac{\partial v}{\partial t} = E\frac{\partial^2 v}{\partial y^2}, \tag{9}$$

a damped wave equation, or the telegraph equation, that has been studied by a number of authors, for example [21]. This equation was also derived in [15] by Denn and Porteous, however, with time scaled by the inertial diffusion time $\rho H^2/\eta_p$ as opposed to the relaxation time λ_{eff}. For a step boundary condition ($v|_{y=0} = H(t)$, where $H(t)$ is the Heaviside step function and $v|_{y=1} = 0$) from rest ($v(y, 0^-) = 0$), the transient response can be represented as $v = e^{-\frac{t}{2}}u(y,t) + 1 - y$, in which the function u satisfies a linear Klein–Gordon equation $u_{tt} - \frac{1}{4}u = Eu_{yy}$. When $E \gg 1$, the solution of the Klein–Gordon equation can be approximated as a traveling wave: $u(y,t) \approx u(y - \sqrt{E}t)$. The evolution of the velocity v is described essentially by a damped traveling wave with dimensionless wave speed $\sqrt{E}$. Of importance to future discussions is that the amplitude of the wave takes two relaxation times to decay by e^{-1}.

If viscous solvent effects ($\beta \neq 0$) are included (but not stress diffusion, $\delta = 0$), then the governing equation (8) is well approximated by

$$\frac{\partial^2 v}{\partial t^2} + \frac{\partial v}{\partial t} = E\beta \frac{\partial^3 v}{\partial y^2 \partial t} + E\frac{\partial^2 v}{\partial y^2}. \tag{10}$$

The equation is now parabolic, albeit with a small parameter in front of the highest order derivative. For a fairly fast ramp-up or even a step at the boundary from rest, $v|_{y=0} = H(t)$ and $v|_{y=1} = 0$, we anticipate a transient wave front traveling from $y = 0$. The sharpness of this "front" decays through the action of viscoelastic effects in the fluid. The solution to this equation was found analytically by Tanner [36], using Laplace transforms, for a semi-infinite domain (the "Rayleigh problem").

We are particularly interested in the case when β is small and the domain is bounded so that, for short times, damped inertio-elastic shear waves travel across the channel and reflect back from the stationary wall. This is the physically relevant limit for micellar solutions. The computed solution is shown in Figure 2. In Figure 2(a) the velocity contours as a function of space and time are shown for $E = 100$ and $\beta = 10^{-4}$. Although (10) is of parabolic type, a shear wave is observed for O(1) times, traveling at a speed $\sqrt{E} = 10$. Because the coefficient of the highest derivative term is much less than unity ($E\beta = 0.01 \ll 1$), diffusive effects are small. The wave is dampened as it travels back and forth between the two boundaries, and after two relaxation times, the velocity profile is close to linear (see Figure 2(c)), that is, $v = 1 - y$. Figure 2(b) shows the velocity gradient contours on a space time plot from $t = 0.2$ to $t = 2.2$. Note that the initially well-defined steep gradient (corresponding to a shock front) propagating across the gap progressively disappears in time as diffusive effects flatten the velocity profile towards its final linear profile.

In order to better understand the relevance of the magnitude of the composite parameter $E\beta$, we compare the results in Figure 2 to the space-time diagrams in Figure 3, in which the velocity profile is evaluated for much larger values of the elasticity number, $E = 10^4$ (3(a)) and $E = 2.5 \times 10^5$ (3(b)), both still for $\beta = 10^{-4}$ (note that for real wormlike micellar solutions the product $E\beta$ is, in fact, much smaller than this). In Figure 3, since $E\beta \geq 1$, although shear wave propagation and reflection can still be identified at early times, the velocity profile diffuses much more rapidly than that observed with the smaller value of $E\beta$ shown in 2(a) (note the total dimensionless elapsed time scale shown in Figures 2(a), 3(a), and 3(b) are markedly different corresponding to $t_{max} = 2, 0.2, 0.04$, respectively). For these larger values of $E\beta$, diffusion dominates at times much smaller than the fluid relaxation time. The product $E\beta = \lambda_{eff}/(\rho H^2/\eta_s)$, where the numerator λ_{eff} is the viscoelastic stress

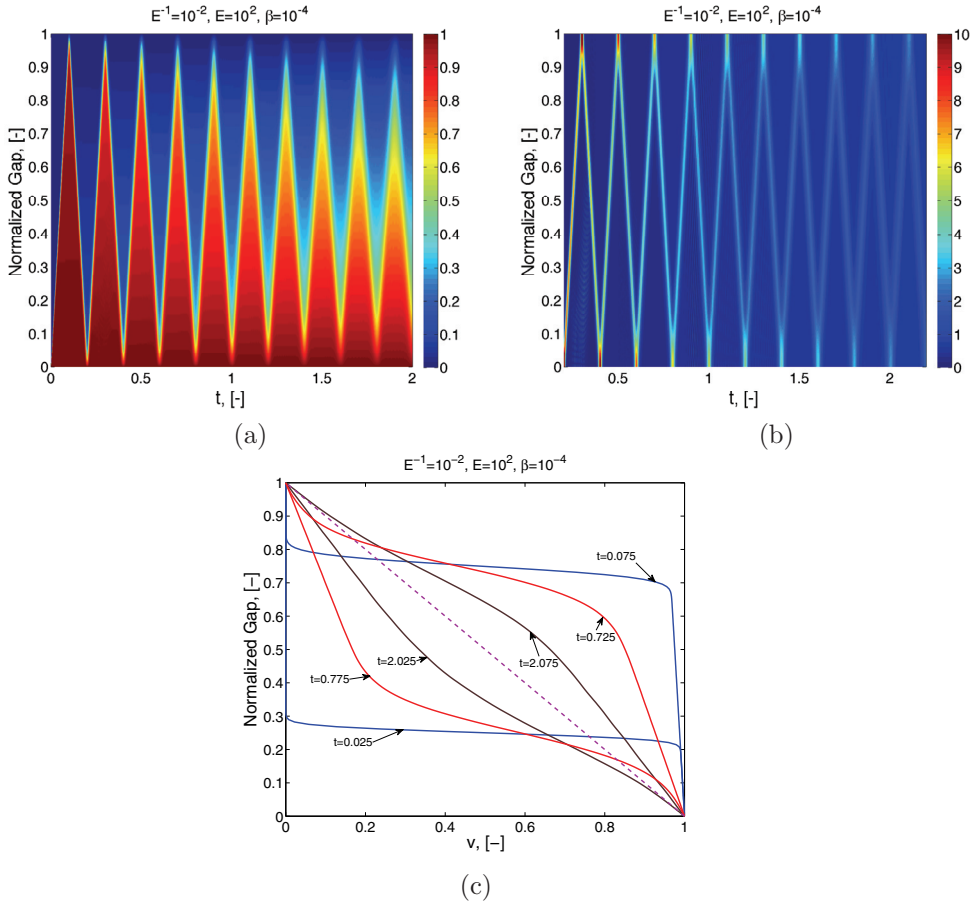

FIG. 2. *Space-time diagram showing the short time transient behavior of the O-B model with a step increase in wall velocity* $v|_{y=0} = H(t)$. (a) *The velocity as a function of position and time is plotted for* $E = 100$, $\beta = 10^{-4}$. (b) *Velocity gradient as a function of position and time for times* $t = 0.2$ *to* $t = 2.2$. (c) *Velocity profiles* $v(y, t_i)$ *as a function of position at selected times* t_i. *The dashed line is the final steady state solution* $v = 1 - y$.

relaxation time scale and the denominator $(\rho H^2/\eta_s)$ measures the diffusion time scale based on the solvent viscosity alone. For $E\beta > 1$, kinematic information regarding the moving boundary travels much more rapidly than elastic stress.

So far, the discussion of the solutions of (10) is based on the boundary condition that at $t = 0^+$, $v = 1$ at the moving wall. This requires the moving wall to reach its maximum velocity instantaneously. However, in actual rheometric experiments, the motor can only ramp up to its final velocity in a finite time. To mimic this response, we impose a time-dependent (ramped) speed $v_i = De \tanh(at)$ for $t \geq 0$ at the moving wall. The dimensionless parameter $a = \lambda_{eff}/t'_{ramp}$ controls the speed at which the imposed velocity reaches its final value: for example, for $a = 100$, it takes 0.025 relaxation times for the moving wall velocity to be at 99% of the final velocity; for a smaller value, say $a = 2.5$, it takes roughly one relaxation time for the moving wall velocity to reach 99% of its final value. In a rheometer, a typical value is $a \sim O(10)$ (in fact $a \approx 25$ as mentioned earlier) [30]. The boundary condition utilized in our initial computations presented in Figures 2 and 3 ($v = 1$ at $t = 0^+$) corresponds to

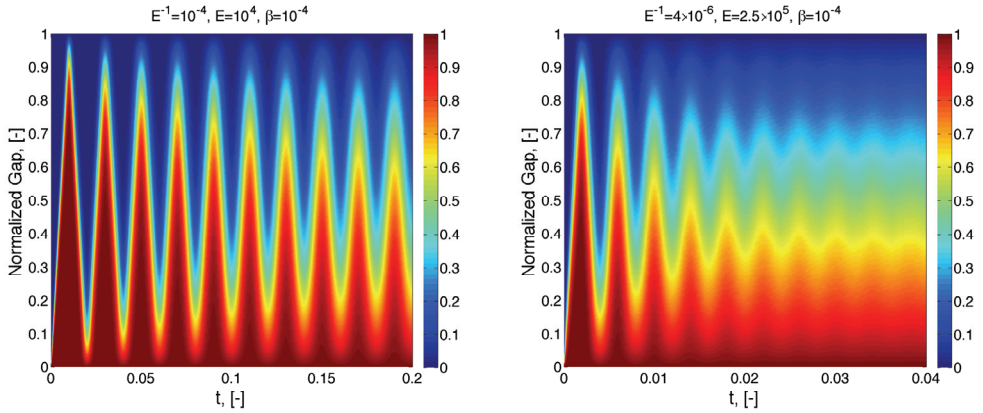

(a) (b)

FIG. 3. *Space-time diagrams showing the effect of increased viscous damping* ($E\beta = \frac{\lambda_{eff}}{(\rho H^2 \eta_s)}$) *on the short time transient behavior of the O-B model with a step increase in wall velocity* $v|_{y=0} = H(t)$. *The velocity as a function of position and time is plotted for the following:* (a) $E = 10^4$, $\beta = 10^{-4}$, (b) $E = 2.5 \times 10^5$, $\beta = 10^{-4}$.

the limiting case of $a \to \infty$ (and $De = 1$), and a fast ramp $a = 100$ should be a good approximation of this limiting case. In Figure 4 we show the time evolution of the velocity across the gap for both the ramp speed of $a = 25$ and a slower ramp speed $a = 5$. For the smaller value of a the velocity ramp up takes about 0.4 relaxation time to reach its limiting value of unity, and thereafter the velocity profile in the fluid exhibits damped oscillations until it finally achieves the fully developed linear profile. For this value of a, the viscoelastic stress in the micellar solution has time to relax as the shear wave propagates and the velocity establishes a linear profile much more rapidly than in the case for the larger a. As a decreases further, e.g., $a = 1$, for the same values of E and β, a viscoelastic shear wave can barely be observed in the transient velocity response.

When all parameters are nonzero, to leading order equation (9) is a beam equation; however, the equation is singularly perturbed, and the effect of the highest order spatial derivative term is not seen in our short time transient ($t = O(1)$) calculations of the O-B model with diffusion. Figure 5 shows several computed profiles up to one relaxation time, $t = 1$, for varying δ in which $E\beta\delta$ ranges from 0 to 10^{-4}. For large elasticity numbers and these small values of diffusivity, the characteristics of the response do not change much by varying δ.

Having demonstrated the essential physical aspects of the quasi-linear governing constitutive equations of the Oldroyd-B model, we now proceed to consider the full nonlinear two species VCM model constitutive equation. As a reminder the E, β, a parameter space of interest for actual wormlike micellar solution is that of Figure 4(a).

4. Transient elastic waves and multiply-banded solutions in the VCM model with fluid inertia.

4.1. Analysis in the absence of stress diffusion. The full coupled set of equations for the VCM model, incorporating the effects of fluid inertia, is solved in a cylindrical Couette geometry as was studied experimentally by Miller and Rothstein [27]. At steady state the inner cylinder rotates at a constant (nondimensional) speed De and the outer cylinder is fixed. In the analysis below, motivated by the results of

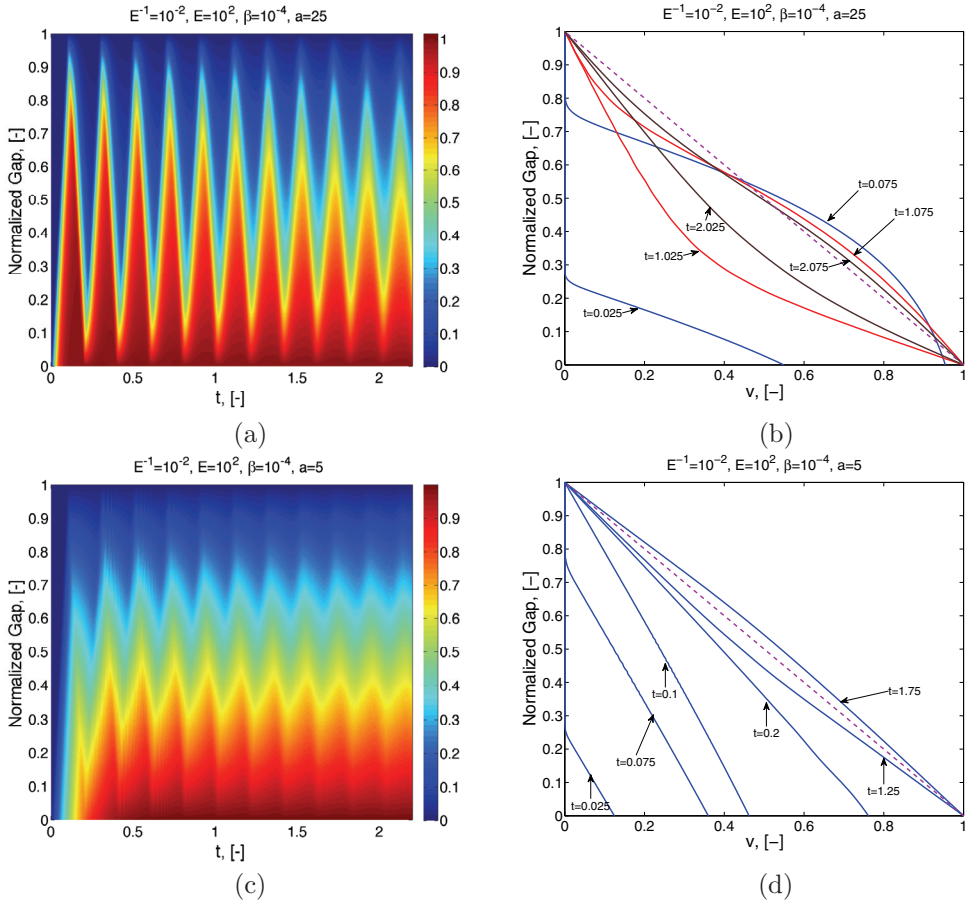

FIG. 4. *Space-time diagram showing the short time transient behavior of the O-B model with the wall velocity ramped up from rest ($v_i = v|_{y=0} = \tanh(at)$), with $E = 10^2$, $\beta = 10^{-4}$, and $a = 25$ (top) corresponding to a fast wall ramp rate, $a = 5$ (bottom) corresponding to a much slower start up of the moving wall.* (a), (c) *The velocity as a function of position and time.* (b), (d) *Velocity profiles $v(y, t_i)$ as a function of position at selected times t_i. The dashed line is the final steady state solution $v = 1 - y$.*

the previous section, we first consider the solutions without diffusion, $\delta_A = \delta_B = 0$ for simplicity, and then consider the effects of including stress diffusion in the model. Note that the VCM model system is of composite type with the stress and momentum subsystem behaving similarly to that of an O-B model discussed above. In our computation of the VCM model, the dimensionless solvent viscosity ratio β is fixed at $\beta = 6.8 \times 10^{-5}$, and p, the curvature of the device, is fixed at $p = 0.1$ [41]. In what follows, y represents the scaled distance from the inner cylinder, i.e., $y = (r' - r'_i)/H$.

Figure 6 shows the dynamic processes leading to the formation of a (regular) two-banded VCM profile: in the top row there is no inertia in the system, $E^{-1} = 0$; in the bottom row there is nonzero but small inertia $E^{-1} = 10^{-3}$, corresponding to a dimensionless wave speed $\sqrt{E} \sim 33$. The left-hand figures are time-space-velocity contour plots, and the right-hand figures display vertical slices through the contour plots; that is, the velocity profile as a function of position across the gap at selected times. For the inertialess fluid (Figure 6 (top)) the wave speed is infinite and the

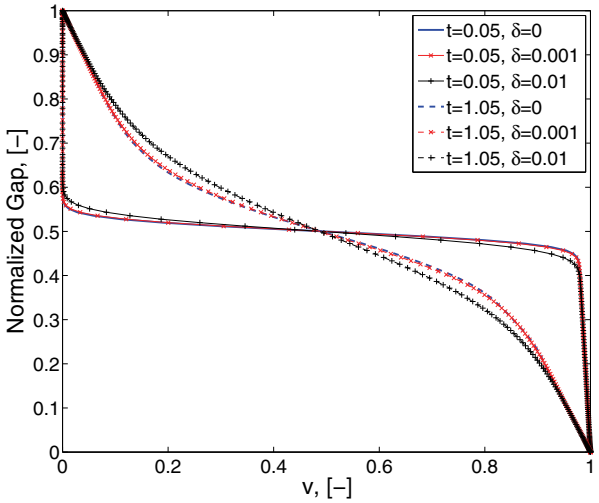

FIG. 5. *Velocity profiles of the O-B model with diffusion at two selected times and several values of the parameter* $E\beta\delta$. $E = 100$, $\beta = 10^{-4}$, *and* $E\beta\delta = 0, 10^{-5}, 10^{-4}$, *affirming the similarity in the profiles for times on the order of one relaxation time.*

initial establishment of a linear profile is controlled purely by the wall ramp rate a. In the figure, $a = 100$, so that it takes a very short time $t \approx 0.01$ to establish a linear velocity profile across the gap. Subsequent nonlinear elastic stress growth distorts this linear profile and ultimately leads to an elastic recoil event at $t \approx 0.25$ (corresponding to a local region of negative velocity). After completing the recoil the velocity slowly settles into its banded steady state with the single sharp kink located at $y_k \approx 0.22$ separating two shear bands. This elastic recoil event has been investigated in several different models [2, 40, 41] and has also been seen in experiments with different types of entangled fluids including monodisperse polymer solutions [7, 37] and micellar solutions [25, 27, 35].

When inertia is included with an elasticity number $E = 1000$ (Figure 6 (bottom)), the steady state solution remains unchanged from the inertialess profile; that is, a regular shear banding profile is ultimately established (with a single kink separating two bands). Comparison of the two contour plots shows that for times larger than $t = 0.2$, the velocity profiles are similar and an elastic recoil event is observed in both. However, the two contour plots show differences in the early time behavior. For $E\beta \ll 1$, there is an initial (damped) wave-like disturbance traveling from one boundary to the other as in the O-B model. While the velocity disturbance formally reaches the outer boundary instantaneously (due to the diffusive nature of the equation) it takes a finite time ($t \sim E^{-1/2} \sim 0.03$) for the velocity to reach a substantial value there. Indeed with this level of inertia a narrow triangular "region of silence" (lower left of Figure 6) is seen at early time near the stationary outer wall indicating this slow transfer of information. As the shear wave speed $\sqrt{E}$ characterizing the propagation of the initial information is decreased, the triangular region of silence broadens in extent as we show in the left-hand column of Figure 7. An additional difference between the two contour plots presented in Figure 6 is the temporal oscillations observed when there is inertia. Before the fluid recoils, a velocity overshoot and undershoot (see Figure 6 (lower right)) can be seen in the profile (at times $t = 0.03, 0.06$, and 0.1). This

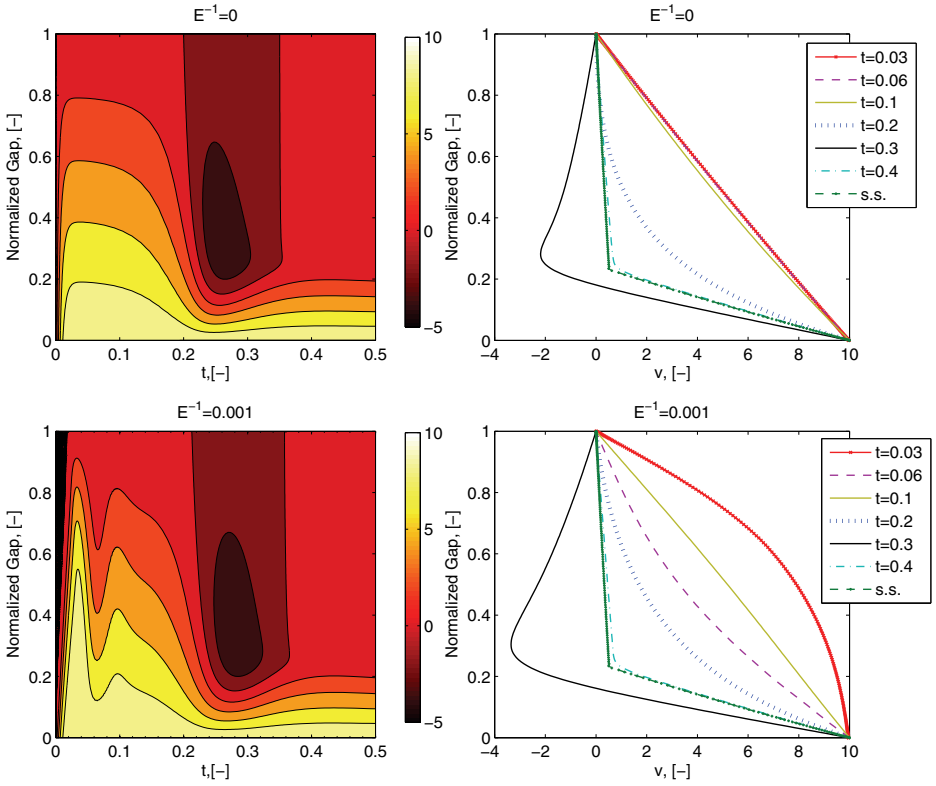

FIG. 6. *Evolution of the velocity profile in time and space for the VCM model with a ramp time of* $a^{-1} = 0.01$ *and* $De = 10$. *The left-hand column shows velocity contours* $v(y,t)$, *and the right-hand column shows the velocity profiles across the gap for selected times. The top row corresponds to no fluid inertia* $E^{-1} = 0$ *and the bottom row to* $E^{-1} = 0.001$.

is a result of interactions of the evolving stress field with the "reflected" waves. By $t = 0.2$, the disturbance has dissipated sufficiently that the residual perturbation to the flow is negligible; after three prominent oscillations, the disturbance to the inertialess flow has disappeared. In particular, the oscillations are completely damped before the elastic recoil event ($t \approx 0.25$) and the steady state solution is not affected. Similar oscillations during the start up of steady shear flow are also observed experimentally by Miller [26].

As E is decreased further from the value used in Figure 6, the influence of the initial boundary disturbance travels more slowly and the shear wave takes longer to dissipate. Figure 7 shows velocity contour plots and velocity profiles for selected times, similar to those of Figure 6, but for several larger values of E^{-1}, namely $E^{-1} = 0.008$ and 0.01. The oscillations remain prominent but now occur on the same time scale as the elastic recoil event ($t \approx 0.25$). This interaction between the reflected boundary disturbance and the system relaxation changes not only the transient velocity contours but also the ultimate steady state velocity profile. For these two values of E, the velocity of the traveling wave is approximately 10 (that is, it takes 0.1 relaxation time for the wave to travel from one boundary to the other or 0.2 relaxation times to reflect back to the inner wall). In the upper figure the multiple banding is still

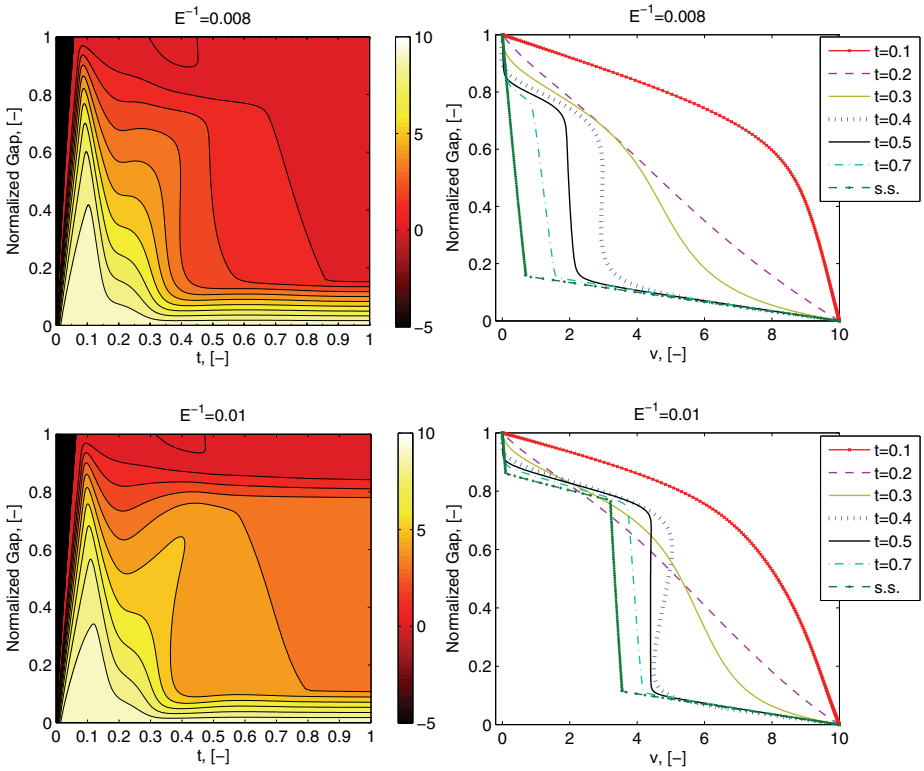

FIG. 7. *Spatio-temporal evolution of the velocity in time for the VCM model with inertia,* $a^{-1} = 0.01$ *and* $De = 10$*; left column, velocity contours as a function of time and space; right column, the corresponding velocity profiles as a function of gap position for selected times. The top row corresponds to* $E^{-1} = 0.008$*, which exhibits regular shear banding (two bands) at steady state, and the bottom row corresponds to* $E^{-1} = 0.01$*, which shows a multiple banding state at steady state with three kinks connecting four distinct regions of different shear rate.*

transient and ultimately the flow evolves to a two-banded state separated by a single kink at $y_k \approx 0.18$. In the lower figure, however, for the slightly smaller value of elasticity number E, the multiple banding persists to steady state.

The analysis presented above shows that in the absence of stress diffusion (i.e., $\delta = 0$) multiple-banded steady state solutions can be attained when inertia in the system is sufficiently large. In the case analyzed above ($De = 10$ and $a = 100$), this corresponds to $E^{-1} \gtrsim 0.008$. A comparison of the analogous results with nonzero stress diffusion follows in section 4.2. Further computations show that a multiple-banded steady state solution exists for a specific range of E^{-1}, and this range is dependent on the transient dynamics of the system of equations and on the values of a, De which characterize the other time scales in the system. In Figure 8(a), the range of E^{-1}, over which the steady state solution shows multiple-banded structures, is plotted as a function of the ramp rate a for selected values of $De \leq 30$. Figure 8(a) shows that there is no multiple banding at steady state, in the case that the inertial diffusion time $t_{idiff} = E^{-1}$ is smaller than a lower critical value denoted by $E_l^{-1}(a^{-1}, De)$, or if E^{-1} is larger than a fixed upper bound (which is dependent

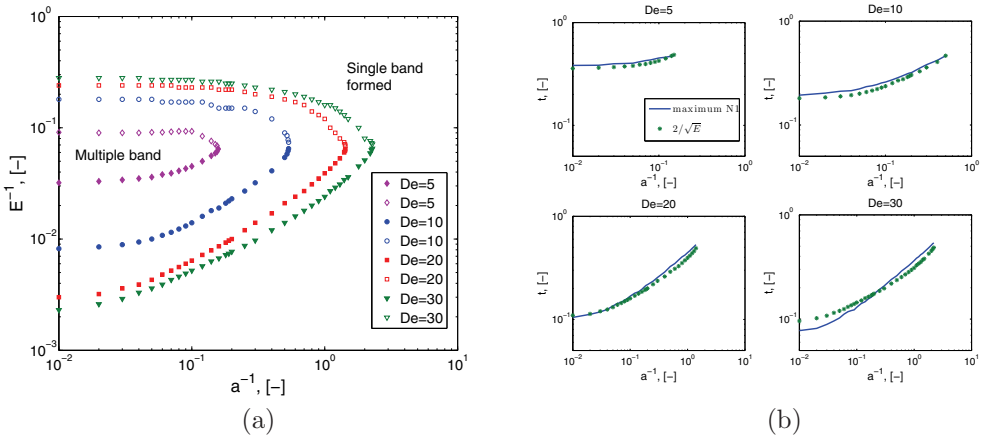

FIG. 8. (a) *Projection of the surface delineating the multiple-banded states on the* $E^{-1} - a^{-1}$ *plane for selected values of the dimensionless wall velocity* $De \leq 30$. (b) *Coupling between normal stress overshoot and shear wave propagation. In each subfigure, the blue (solid) line is the time* t_1 *at which the first normal stress difference* $N_1(t)$ *of the inertialess VCM model passes through a local maximum at each value of the ramp rate, an indicator that the inertialess system is starting to form a shear band. The asterisk indicates the time* $t_2 = 2/\sqrt{E_l}$ *at which the reflected shear wave first returns to the moving surface.*

on De). These boundaries define the extent of the multiple banding region and correspond to the condition that the time scale for propagation of the viscoelastic shear wave be on the same order of the system relaxation time as well as the additional requirement that the inertial diffusion time is not too small relative to the system start-up time. If the inertial diffusion time scale becomes larger than the upper boundary shown in Figure 8(a), multiple banding never occurs because the reflected wave returns after the elastic recoil has already occurred and the steady two-banded solution has been established. For $a^{-1} \gtrsim 1$ (right-hand region of Figure 8(a)) and the values of De considered here, the transient inertio-elastic waves damp out before the start-up ramp is complete so the traveling wave cannot interfere with the formation of the two-banded profile. This means no multiple banding steady state solutions exist for any value of E .

For this range of wall speeds ($De \leq 30$) the critical value of the wave speed corresponding to the onset of the multiple banding (i.e., the lower boundary of the multiple banding region in Figure 8(a)) can be understood in terms of the recoil time of the inertialess flow. In a previous paper [41] it was shown, for a simpler (but still nonlinear) limiting version of the VCM model, that the time at which the recoil occurs coincides with the time at which the first normal stress difference $N_1(\dot{\gamma}, t)$ in the fluid reaches its peak value. The first normal stress difference, defined as $N_1 = \tau_{\theta\theta} - \tau_{rr}$, is a measure of the nonlinear elasticity of the fluid. In each subfigure of Figure 8(b) the time at which the first normal stress difference reaches its maximum overshoot (blue (solid) line) is plotted as a function of a^{-1} for the *inertialess* VCM model at wall speeds $De = 5, 10, 20, 30$. For faster ramps and larger velocities this time becomes progressively shorter. On the same plot the value of $2/\sqrt{E_l}$ (green (asterisk)) is plotted for each De, where E_l^{-1} is the lower boundary of the multiple banding region shown in Figure 8(a) when inertia is included. This is the time it takes for the elastic wave to travel across the gap and reflect back to the inner cylinder. At these short times and for these values of E, the wave doesn't dampen substantially. The good agreement of these two

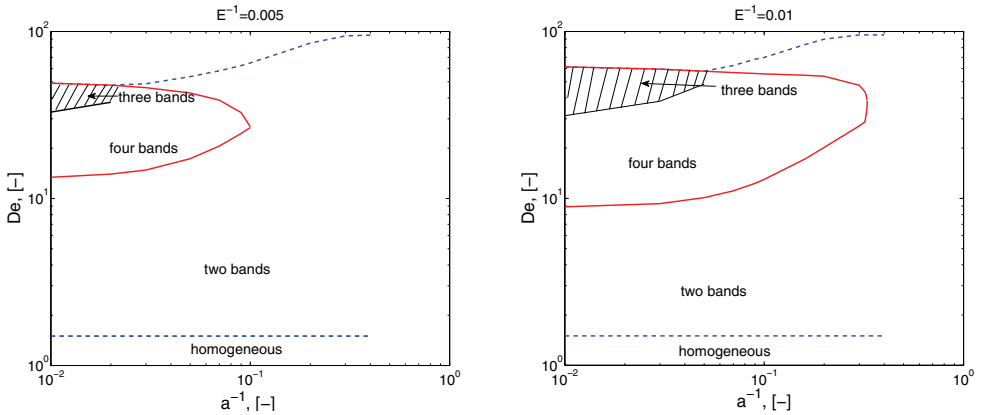

FIG. 9. *Projection of the surface delineating the multiple-banded states on the shear rate (De), start-up rate (a^{-1}) plane for two selected values of the elasticity number: $E^{-1} = 0.005$ (a) and $E^{-1} = 0.01$ (b) indicating the domains where the final velocity profiles exhibit no bands (i.e., homogeneous shearing flow), two bands (enclosed by blue (dashed) lines), four bands (red (enclosed) region), and three bands (hashed region).*

times indicates that for $De < 30$, the creation of multiple shear bands at steady state is due to the interaction of the undamped traveling wave with the elastic recoil in the system arising from the transient overshoot in the elastic normal stress difference.

When the wall velocity De increases further, the traveling wave affects the final solution structure in a more complicated way: not only are four-banded solutions (corresponding to high-low-high-low shear rate) observed, but also three-banded (high-low-high shear rates) solutions are observed. This can be seen by examining the structure of the results in De versus a^{-1} space for a fixed value of E. Figure 9 shows such projections for two specific cases $E^{-1} = 0.005$ and $E^{-1} = 0.01$. Comparing these two figures, it is clear that as E^{-1} increases (i.e., inertial effects become increasingly pronounced), the multiple banding region (region enclosed by the red (solid) lines) gets larger. In both figures, for very fast ramp up boundary conditions (i.e., $a^{-1} \to 0$), as De increases, the solution first shows a two-banded solution, then a four-banded solution, and finally a three-banded solution before all banding is eliminated. Figure 10(a) shows the corresponding steady state velocity profiles of the case when $a^{-1} = 0.01$ for selected increasing values of the dimensionless wall velocity, De. By contrast, for intermediate ramp-up speeds, the three-banded solution is eliminated and the velocity profile in the gap passes directly from a four-banded solution to a regular two-banded solution before banding disappears. Figure 10(b) shows the corresponding steady state velocity profiles for the case when the ramp rate is slower $a^{-1} = 0.1$ and the dimensionless wall velocity is incremented.

To see more clearly the evolution in the banding structure of the different cases in Figure 10, the transition of the kink locations (corresponding to interfaces between the different dynamical "phases") through parameter space for these two cases ($E^{-1} = 0.01$, and $a^{-1} = 0.01$ or 0.1) are plotted in Figure 11. The dashed black line is the kink location in the inertialess limit $E^{-1} = 0$. In this limit the kink location $y_k(De)$ moves almost linearly across the gap as the wall velocity increases corresponding to an approximate "lever rule" [18, 34]. For the value of $E^{-1} = 0.01$ used in the calculations, and the faster ramp ($a^{-1} = 0.01$), the system transitions from a two-banded to a four-

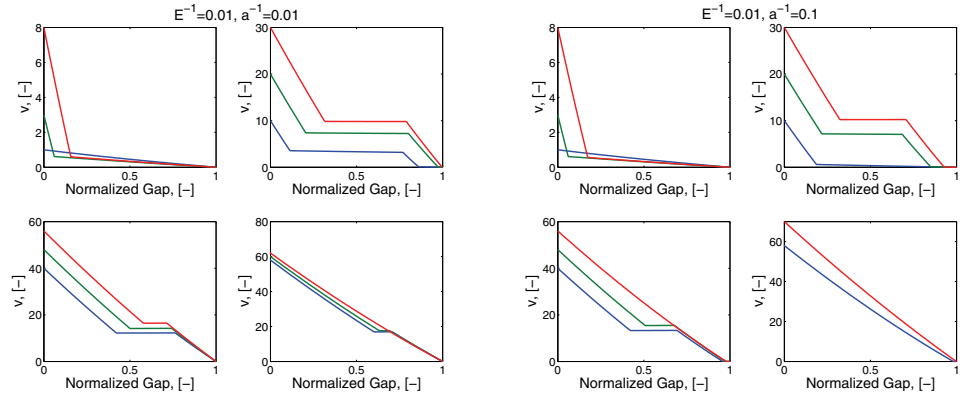

FIG. 10. *The steady state velocity profiles across the gap for the VCM model with increasing wall velocities ($v(y = 0) = De$):* (a) *linear, two-banded, four-banded, three-banded, linear;* (b) *linear, two-banded, four-banded, two-banded, linear.*

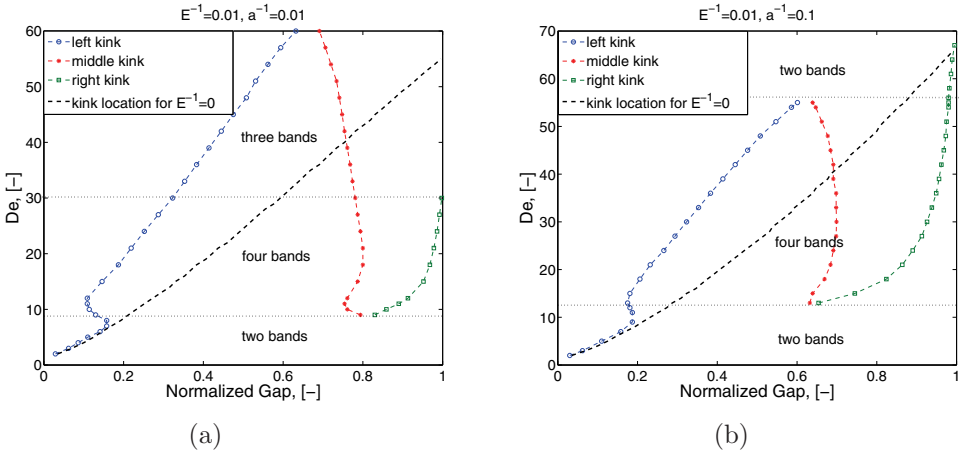

FIG. 11. *Movement of the kink positions shown in Figures* 10(a) *and* (b) *as the effective shear rate increases. Notice that when $a^{-1} = 0.01$, the uppermost kink merges with the wall when $De > 30$, diminishing the number of bands from four to three.*

banded state as De increases with the two new interfaces developing towards the outer stationary wall ($y \approx 0.8$). As the wall velocity increases further the outermost interface moves towards the outer stationary wall where it eventually terminates (at $De \approx 30$) returning the system to a three-banded state. The remaining two interfaces eventually merge so that the system returns to a homogeneous unbanded state for $De > 65$. Similarly, under the influence of the slower ramp ($a^{-1} = 0.1$) as De increases, the two-banded state transitions to a four-banded state; however, in this case no three-banded state is seen as De increases further. The two innermost interfaces eventually merge (at $De \approx 57$) leaving only the outermost interface corresponding to the classical two-banded state with the single kink location close to the outer stationary wall.

4.2. The singular role of stress diffusion. When the stress diffusion parameter δ is small but nonzero, the transient band evolution initially follows the same

trajectory evaluated for the zero stress diffusion case ($\delta = 0$), creating multiple-banded states at the recoil time. Thereafter, slow diffusive processes take over so that ultimately, at steady state, only the two-banded profile remains. Figure 12(a) shows the time evolution of a typical multiple-banded profile for short times $t \leq 0.6$ and the steady state when the dimensionless diffusion parameter is $\delta = 0.1$. Note that after the interaction of the reflected wave and the elastic recoil, multiple-banded profiles are observed with the sharp interface between neighboring bands now smoothed out by stress diffusion. The extent of the leftmost (low shear rate) band slowly decays until it reaches its final state. As the velocity of this low shear rate band decreases, the rightmost high shear rate band disappears as the two low shear rate bands merge. The nonlinear VCM model involves two micellar species, a long species A which breaks at a rate that increases with shear rate into two of the short species B worms. In Figure 12(b) we show the time evolution of the number density of species A across the gap. The number density of long species is low in the high shear rate region but is closer to its equilibrium value $n_A = 1$ in the low shear rate region.

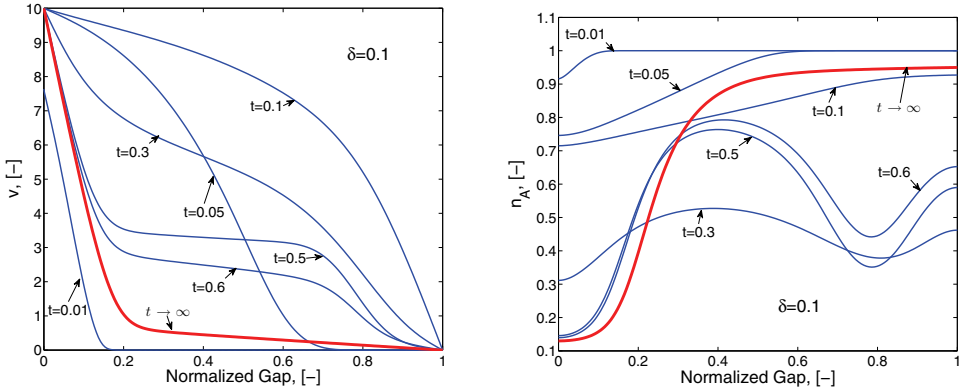

FIG. 12. (a) *The transient velocity and* (b) *the number density of species A are plotted as functions of space for selected times for the VCM model with fluid inertia when stress diffusion is included. In both plots,* $E = 100, a^{-1} = 0.01, De = 10,$ *and* $\delta_A = \delta_B = 0.1$.

The rate of decay of the leftmost low shear rate band is directly controlled by the magnitude of the stress diffusion parameter δ. To illustrate this dependence, we show in Figure 13(a) a characteristic velocity in the leftmost low shear rate band as a function of time ($v(t)|_{y=0.5}$) for several different diffusion parameters for a fixed wall speed $De = 10$, elasticity number $E = 100$, and ramp rate $a = 100$. Note that as δ decreases, the time to reach the steady state (two-banded profile) increases. In the limiting case when $\delta = 0$, the solution never reaches a two-banded profile. Figure 13(b) shows the time it takes for the velocity at the midplane $v(t)|_{y=0.5}$ to decay to its steady state value as a function of the magnitude of the stress diffusion parameter. Note that the plot is a straight line over most of the range with a slope of $-1/2$, indicating a dimensionless decay time scales as $\delta^{-\frac{1}{2}}$ and is consequently much longer than the viscoelastic relaxation time. Long time-scale transients are often observed in experimental measurements with wormlike micellar solutions following inception of steady shear flow [19, 30].

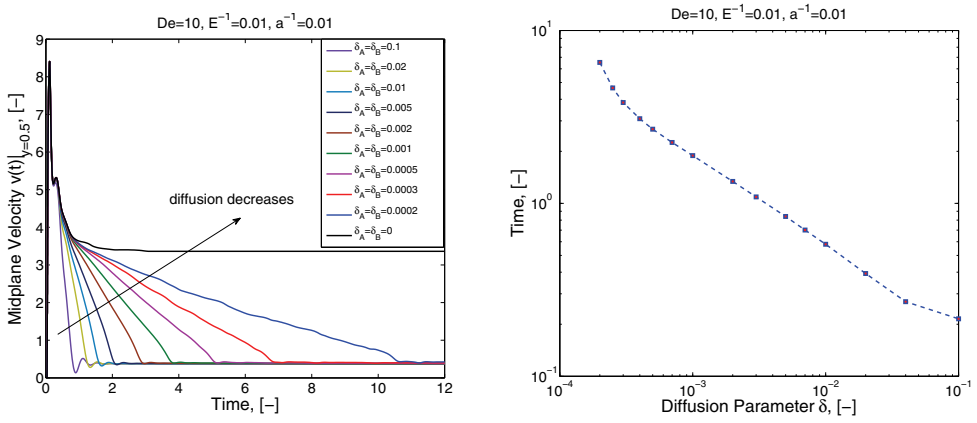

(a) (b)

FIG. 13. (a) *The velocity at the middle plane* $v(t)|_{y=0.5}$ *for the inertial VCM model with nonzero stress diffusion parameter is plotted as a function of time for different values of the dimensionless diffusivity* δ. (b) *The time it takes for the velocities in* (a) *to decay to the steady state value is plotted for different values of the stress diffusion parameter. In both plots,* $E = 100, a^{-1} = 0.01, De = 10$.

5. Conclusion. In this paper the effect of fluid inertia and the stress diffusion on the transient shear banding dynamics exhibited by the VCM model for wormlike micellar solutions has been explored. The presence of fluid inertia leads to the transient propagation of damped inertio-elastic shear waves with a finite wave speed given (in dimensional terms) by $c' = \sqrt{G/\rho}$, or in dimensionless terms by $c = \sqrt{E}$. This wave decays due to the fluid viscoelasticity over a time scale of several relaxation times. If the diffusive effects of the viscous solvent are sufficiently small ($\beta \ll 1$), then the wave reflects off the inner surface and can interact with the processes leading to the formation of shear bands. Of particular note, we find that the shear-banding structure observed for inertialess flow (which consists of two distinct shear bands) can be disrupted to result in three-banded or four-banded transient solutions. These multiple-banded solutions persist to steady state if the stress diffusion is zero; otherwise they eventually decay back to the two-banded velocity profile on very long time scales $t' \sim \lambda_{eff}/\sqrt{\delta}$. There are a number of important dimensionless parameters and time scales in this problem which affect this phenomenon including the time it takes to ramp the driving wall up to steady state (a^{-1}), the effective relaxation time of the micellar fluid (λ_{eff}), and the magnitude of the inertial terms in the equation of motion (characterized by the inverse of the elasticity number $E = \lambda_{eff}\eta_p/\rho H^2$). The interactions between these competing effects can be represented in a three-dimensional state diagram involving the parameters a^{-1}, E^{-1} and the dimensionless wall speed $De = \lambda_{eff}U/H$. Orthogonal projections of this state diagram and the corresponding locus of two-banded, three-banded, and four-banded velocity profiles are shown in Figures 8(a) and 9. Incorporating realistic values for the dimensionless parameter that couples the nonlocal diffusion of stress and number density of species gives rise to very long time transients that are reminiscent of those documented experimentally [19, 30] in wormlike micellar solutions. The inertial VCM model thus appears to be able to capture, at least qualitatively, many of the the complex spatio-temporal dynamical features that have been reported in transient shear flows of entangled micellar fluids.

REFERENCES

[1] J.M. Adams, S.M. Fielding, and P.D. Olmsted, *The interplay between boundary conditions and flow geometries in shear banding: Hysteresis, band configurations, and surface transitions*, J. Non-Newtonian Fluid Mech., 151 (2008), pp. 101–118.

[2] J.M. Adams, S.M. Fielding, and P.D. Olmsted, *Transient shear banding in entangled polymers: A study using the rolie-poly model*, J. Rheol., 55 (2011), pp. 1007–1032.

[3] N. Aksel, C. Fetecau, and M. Scholle, *Starting solutions for some unsteady unidirectional flows of Oldroyd-B fluids*, Z. Angew. Math. Phys., 57 (2006), pp. 815–831.

[4] L. Becu, S. Manneville, and A. Colin, *Spatiotemporal dynamics of wormlike micelles under shear*, Phys. Rev. Lett., 93 (2004), 018301.

[5] A.V. Bhave, R.C. Armstrong, and R.A. Brown, *Kinetic theory and rheology of dilute, nonhomogeneous polymer solutions*, J. Chem. Phys., 95 (1991), pp. 2988–3000.

[6] R.B. Bird, C.F. Curtiss, R.C. Armstrong, and O. Hassager, *Dynamics of Polymeric Liquids: Vol.* 2*, Kinetic Theory*, 2nd ed., John Wiley and Sons, New York, 1987.

[7] P.E. Boukany and S-Q. Wang, *Use of particle-tracking velocimetry and flow birefringence to study nonlinear flow behavior of entangled wormlike micellar solution: From wall slip, bulk disentanglement to chain scission*, Macromolecules, 41 (2008), pp. 1455–1464.

[8] P.T. Callaghan, *Rheo NMR and shear banding*, Rheol. Acta, 47 (2008), pp. 243–255.

[9] M.E. Cates and S.M. Fielding, *Rheology of giant micelles*, Adv. in Phys., 55 (2006), pp. 799–879.

[10] L.P. Cook and L.F. Rossi, *Slippage and migration in models of dilute wormlike micellar solutions and polymeric fluids*, J. Non-Newtonian Fluid Mech., 116 (2004), pp. 347–369.

[11] M. Cromer, L.P. Cook, and G.H. McKinley, *Extensional flow of wormlike micelles*, Chem. Eng. Sci., 64 (2009), pp. 4588–4596.

[12] M. Cromer, L.P. Cook, and G.H. McKinley, *Interfacial instability of pressure-driven channel flow for a two-species model of entangled wormlike micellar solutions*, J. Non-Newtonian Fluid Mech., 166 (2011), pp. 566–577.

[13] M. Cromer, L.P. Cook, and G.H. McKinley, *Pressure-driven flow of wormlike micellar solutions in rectilinear microchannels*, J. Non-Newtonian Fluid Mech., 166 (2011), pp. 180–193.

[14] C.J. Davies, A.J. Sederman, C.J. Pipe, G.H. McKinley, L.F. Gladden, and M.L. Johns, *Rapid measurement of transient velocity evolution using GERVAIS*, J. Magn. Reson., 202 (2010), pp. 93–101.

[15] M.M. Denn and K.C. Porteous, *Elastic effects in flow of viscoelastic liquids*, The Chemical Eng. J., 2 (1971), pp. 280–286.

[16] C.J. Dimitriou, L. Casanellas, T.J. Ober, and G.H. McKinley, *Rheo-PIV of a shear-banding wormlike micellar solution under large amplitude oscillatory shear*, Rheol. Acta, 51 (2012), pp. 395–411.

[17] A.W. El-Kareh and L.G. Leal, *Existence of solutions for all Deborah numbers for a non-Newtonian model modified to include diffusion*, J. Non-Newtonian Fluid Mech., 33 (1989), pp. 257–287.

[18] M.A. Fardin, T.J. Ober, C. Gay, G. Gregoire, G.H. McKinley, and S. Lerouge, *Potential "ways of thinking" about the shear-banding phenomenon*, Soft Matter, 8 (2012), pp. 910–922.

[19] C. Grand, J. Arrault, and M.E. Cates, *Slow transients and metastability in wormlike micelle rheology*, J. Phys. II France, 7 (1997), pp. 1071–1086.

[20] T. Hayat, A.M. Siddiqui, and S. Asghar, *Some simple flows of an Oldroyd-B fluid*, Internat. J. Eng. Sci., 39 (2001), pp. 135–147.

[21] D.D. Joseph, *Fluid Dynamics of Viscoelastic Liquids*, Springer-Verlag, New York, 1990.

[22] S. Lerouge and J-F. Berret, *Shear-induced transitions and instabilities in surfactant wormlike micelles*, Adv. Polym. Sci., 230 (2010), pp. 1–71.

[23] C.-Y.D. Lu, P.D. Olmsted, and R.C. Ball, *Effects of nonlocal stress on the determination of shear banding flow*, Phys. Rev. Lett., 84 (2000), pp. 642–645.

[24] S. Manneville, A. Colin, G. Waton, and F. Schosseler, *Wall slip, shear banding, and instability in the flow of a triblock copolymer micellar solution*, Phys. Rev. E, 75 (2007), 061502.

[25] S. Manneville, J.B. Salmon, L. Becu, A. Colin, and F. Molino, *Inhomogeneous flows in sheared complex fluids*, Rheol. Acta, 43 (2004), pp. 408–416.

[26] E. Miller, *private communications*.

[27] E. Miller and J.P. Rothstein, *Transient evolution of shear banding in wormlike micelle solutions*, J. Non-Newtonian Fluid Mech., 143 (2007), pp. 22–37.

[28] P.D. Olmsted, O. Radulescu, and C.-Y.D. Lu, *Johnson-Segalman model with a diffusion term in cylindrical Couette flow*, J. Rheol., 44 (2000), pp. 257–275.
[29] P.D. Olmsted, *Perspectives on shear banding in complex fluids*, Rheol. Acta, 47 (2008), pp. 283–300.
[30] C.J. Pipe, N.J. Kim, P.A. Vasquez, L.P. Cook, and G.H. McKinley, *Wormlike micellar solutions* II: *Comparison between experimental data and scission model predictions*, J. Rheol., 54 (2010), pp. 881–914.
[31] O. Radulescu and P.D. Olmsted, *Matched asymptotic solutions for the steady banded flow of the diffusive Johnson-Segalman model in various geometries*, J. Non-Newtonian Fluid Mech., 91 (2000), pp. 143–164.
[32] K.R. Rajagopal, *A note on unsteady unidirectional flows of a non-Newtonian fluid*, Int. J. Non-Linear Mech., 17 (1982), pp. 369–373.
[33] H. Rehage and H. Hoffmann, *Rheological properties of viscoelastic surfactant systems*, J. Phys. Chem., 92 (1988), pp. 4712–4719.
[34] J.P. Rothstein, *Strong flows of viscoelastic wormlike micelle solutions*, Rheol. Rev., (2008), pp. 1–46.
[35] J.B. Salmon, A. Colin, S. Manneville, and F. Molino, *Velocity profiles in shear-banding wormlike micelles*, Phys. Rev. Lett., 90 (2003), 228303.
[36] R.I. Tanner, *Note on the Rayleigh problem for a visco-elastic fluid*, Z. Angew. Math. Phys., 13 (1962), pp. 573–580.
[37] P. Tapadia and S-Q. Wang, *Direct visualization of continuous simple shear in non-Newtonian polymeric fluids*, Phys. Rev. Lett., 96 (2006), 016001.
[38] P.A. Vasquez, G.H. McKinley, and L.P. Cook, *A network scission model for wormlike micellar solutions* I: *Model formulation and homogeneous flow predictions*, J. Non-Newtonian Fluid Mech., 144 (2007), pp. 122–139.
[39] H.J. Wilson and S.M. Fielding, *Linear instability of planar shear banded flow of both diffusive and non-diffusive Johnson-Segalman fluids*, J. Non-Newtonian Fluid Mech., 138 (2006), pp. 181–196.
[40] L. Zhou, L.P. Cook, and G.H. McKinley, *Probing shear-banding transitions of the VCM model for entangled wormlike micellar solutions using large amplitude oscillatory shear (LAOS) deformations*, J. Non-Newtonian Fluid Mech., 165 (2010), pp. 1462–1472.
[41] L. Zhou, P.A. Vasquez, L.P. Cook, and G.H. McKinley, *Modeling the inhomogeneous response and formation of shear bands in steady and transient flows of entangled liquids*, J. Rheol., 52 (2008), pp. 591–623.